


RESEARCH

Open Access



Lysophosphatidic acid as a CSF lipid in posthemorrhagic hydrocephalus that drives CSF accumulation via TRPV4-induced hyperactivation of NKCC1

Trine L. Toft-Bertelsen¹, Dagne Barbuskaite¹, Eva Kjer Heerfordt¹, Sara Diana Lolansen¹, Søren Norge Andreassen¹, Nina Rostgaard², Markus Harboe Olsen³, Nicolas H. Norager², Tenna Capion², Martin Fredensborg Rath¹, Marianne Juhler^{2,4} and Nanna MacAulay^{1*} 

Abstract

Background: A range of neurological pathologies may lead to secondary hydrocephalus. Treatment has largely been limited to surgical cerebrospinal fluid (CSF) diversion, as specific and efficient pharmacological options are lacking, partly due to the elusive molecular nature of the CSF secretion apparatus and its regulatory properties in physiology and pathophysiology.

Methods: CSF obtained from patients with subarachnoid hemorrhage (SAH) and rats with experimentally inflicted intraventricular hemorrhage (IVH) was analyzed for lysophosphatidic acid (LPA) by alpha-LISA. We employed the *in vivo* rat model to determine the effect of LPA on ventricular size and brain water content, and to reveal the effect of activation and inhibition of the transient receptor potential vanilloid 4 (TRPV4) ion channel on intracranial pressure and CSF secretion rate. LPA-mediated modulation of TRPV4 was determined with electrophysiology and an *ex vivo* radio-isotope assay was employed to determine the effect of these modulators on choroid plexus transport.

Results: Elevated levels of LPA were observed in CSF obtained from patients with subarachnoid hemorrhage (SAH) and from rats with experimentally-inflicted intraventricular hemorrhage (IVH). Intraventricular administration of LPA caused elevated brain water content and ventriculomegaly in experimental rats, via its action as an agonist of the choroidal transient receptor potential vanilloid 4 (TRPV4) channel. TRPV4 was revealed as a novel regulator of ICP in experimental rats via its ability to modulate the CSF secretion rate through its direct activation of the Na⁺/K⁺/2Cl⁻ cotransporter (NKCC1) implicated in CSF secretion.

Conclusions: Together, our data reveal that a serum lipid present in brain pathologies with hemorrhagic events promotes CSF hypersecretion and ensuing brain water accumulation via its direct action on TRPV4 and its downstream regulation of NKCC1. TRPV4 may therefore be a promising future pharmacological target for pathologies involving brain water accumulation.

*Correspondence: macaulay@sund.ku.dk

¹ Department of Neuroscience, Faculty of Health and Medical Sciences, University of Copenhagen, Blegdamsvej 3, 2200 Copenhagen, Denmark
Full list of author information is available at the end of the article



© The Author(s) 2022. **Open Access** This article is licensed under a Creative Commons Attribution 4.0 International License, which permits use, sharing, adaptation, distribution and reproduction in any medium or format, as long as you give appropriate credit to the original author(s) and the source, provide a link to the Creative Commons licence, and indicate if changes were made. The images or other third party material in this article are included in the article's Creative Commons licence, unless indicated otherwise in a credit line to the material. If material is not included in the article's Creative Commons licence and your intended use is not permitted by statutory regulation or exceeds the permitted use, you will need to obtain permission directly from the copyright holder. To view a copy of this licence, visit <http://creativecommons.org/licenses/by/4.0/>. The Creative Commons Public Domain Dedication waiver (<http://creativecommons.org/publicdomain/zero/1.0/>) applies to the data made available in this article, unless otherwise stated in a credit line to the data.

Keywords: Transient receptor potential vanilloid 4, Choroid plexus, LPA, Membrane transport, Intraventricular hemorrhage, IVH, SAH, Subarachnoid hemorrhage, Cerebrospinal fluid, Brain water

Introduction

The mammalian brain is submerged in cerebrospinal fluid (CSF), the majority of which is continuously produced by the choroid plexus, a monolayered epithelial structure that protrudes from the ventricular wall [1, 2]. The CSF serves crucial roles such as cushioning the brain and thus protecting it from mechanical insult [3] in addition to acting as the transport route for delivery/disposal of nutrients, metabolites, and immune modulators [4]. Dysregulation of CSF dynamics occurs in a range of neuropathologies, among others posthemorrhagic hydrocephalus (PHH) [5–7], in which water accumulates in the brain after the hemorrhagic event, causing ventriculomegaly and elevation of the intracranial pressure (ICP). PHH may arise secondary to spontaneous or traumatic intracranial hemorrhage in all age groups [8, 9], particularly frequently following hemorrhage in the subarachnoid and ventricular compartments. Such pathological posthemorrhagic brain water accumulation is generally attributed to impaired clearance of CSF caused by obstruction of CSF flow pathways. Currently, the only available treatment relies on drainage of the excess fluid from the brain via surgical CSF diversion through external ventricular drainage, ventricular shunt placement or ventriculostomy [10, 11]. These surgical procedures associate with frequent side effects, i.e. infections and shunt malfunctions, which necessitate alternative treatment options. However, pharmacological interventions have proven suboptimal [12, 13], partly due to the knowledge gap concerning the molecular mechanisms of CSF secretion and their regulatory properties in health and disease.

The serum lipid lysophosphatidic acid (LPA) [14] enters the brain with hemorrhagic events, such as during traumatic brain injury and a murine model thereof [15]. LPA appears to worsen the outcome in the process [15], as it does in neonatal mice models [16, 17]. These mouse models of (embryonic or postnatal) PHH displayed a range of LPA-mediated morphological changes in the week(s) following intracranial LPA administration, such as ventricular enlargements, 3rd ventricular occlusion, elevated ICP, thinning of cortical layers, and cilia loss along the lateral ventricular walls [16, 17]. LPA effectuated these features via their G protein-coupled LPA receptors expressed in the brain tissue (LPA_{R1}-LPA_{R6}) [16–18] and thus appear to act as a key factor in the etiology of PHH.

Emerging evidence suggests a component of CSF hypersecretion in some forms of hydrocephalus in patients and experimental animal models, i.e. choroid

plexus hyperplasia, choroid plexus tumours, or PHH [5, 6, 19]. In the rodent experimental model of intraventricular hemorrhage (IVH), the PHH was demonstrated to occur following CSF hypersecretion [6]. The molecular coupling between the hemorrhagic event and the hydrocephalus formation was proposed to rely on the associated inflammatory response activating the Toll-like Receptor 4 (TLR4) signalling pathway, which ultimately promoted hyperactivity of the choroidal Na⁺/K⁺/2Cl⁻ cotransporter NKCC1 [6], that serves as a key contributor to CSF formation by rodent and canine choroid plexus [6, 20–22]. Hemorrhage-induced CSF hypersecretion may, in addition, be promoted by the LPA entrance occurring with the brain insult.

The choroid plexus epithelial cells abundantly express the Ca²⁺-permeable nonselective cation channel transient receptor potential vanilloid 4 (TRPV4) [23, 24]. TRPV4 is polymodal in a sense of its several distinct manners of activation, one of which being lipid-mediated modulation of channel activity [25]. TRPV4 has been implicated in CSF secretion following demonstration of its ability to modulate transepithelial ion flux in choroid plexus cell lines [26, 27] and of TRPV4 antagonists effectively alleviating ventriculomegaly in a genetic animal model of hydrocephalus [28]. TRPV4 could thus act as the molecular link coupling the hemorrhage-mediated LPA elevation to the CSF hypersecretion and ensuing hydrocephalus.

Here, we demonstrate that LPA is indeed elevated in patients with subarachnoid haemorrhage (SAH) and in an animal model of IVH and reveal its ability to directly modulate the ion channel TRPV4, which subsequently promotes NKCC1-mediated CSF hypersecretion and ventriculomegaly.

Methods

Patients

CSF samples were collected between June 2019 and September 2021 from 12 patients (mean age: 63 y, range: 40–77 y, 7 F/ 5 M) with acute SAH admitted and treated for the condition at Department of Neurosurgery at Rigshospitalet, Copenhagen, Denmark. CSF samples were obtained within 48 h of ictus (n=12, see Additional file 1: A for LPA levels as a function of time from ictus to CSF sampling) through an external ventricular drain (EVD) inserted on clinical indications. To exclude that measured CSF parameters could be affected by neuroinfections requiring antibiotic treatment, patients with no

signs of neuroinfection at admission or during their treatment were selected. All included patients later received a permanent ventriculo-peritoneal shunt because of continued need for CSF diversion. As control subjects, 14 patients undergoing preventive surgery for unruptured aneurysms (vascular clipping) were enrolled (mean age: 61 y, range: 39–71 y, 8 F/6 M), and CSF was collected from the basal cisterns during surgery prior to clipping of the aneurysm. CSF was collected in polypropylene tubes (Sarstedt), centrifuged at $2000\times g$ for 10 min at 4 °C, split into aliquots, and stored at –80 °C no later than 2 h after collection and until quantification of LPA (see below). Written informed consent were obtained from all patients or next of kin depending on the capacity of the patients and the study was approved by the Ethics committee of the Capital Region of Denmark (H-19001474/69197/H-17011472).

Animals

All animal experiments complied with the relevant ethical regulations and conformed to European guidelines. The Danish Animal Experiments Inspectorate approved the experiments (permission no. 2016-15-0201-00944 and 2018-15-0201-01595). Adult male Sprague Dawley rats (Janvier Labs) of 9 weeks used for the animal experimentation were housed with a 12:12 light cycle and access to water and food *ad libitum* accordingly to the ARRIVE guidelines. Animals were ordered weekly from the supplier for a specific set of experiments and randomized within the group and evenly distributed to each of the experimental conditions.

Anaesthesia and physiological parameters

The experimental animals were anaesthetized with intraperitoneal (i.p.) injection with 6 mg ml⁻¹ xylazine + 60 mg ml⁻¹ ketamine (ScanVet) in sterile water (0.17 ml per 100 g body weight, pre-heated to 37 °C). Animals were re-dosed with half ketamine dose as required to sustain anaesthesia. Animals were excluded if they did not respond to the anaesthesia regimen immediately (for the live imaging of the CSF secretion experiments, where the animals were not ventilated) or within the first three re-dosings (for the ventriculo-cisternal perfusion assay (see below) and ICP measurements, where the animals were mechanically ventilated). Such events occurred rarely. Isoflurane (1000 mg g⁻¹, ScanVet) was employed for survival procedures (mixed with 1.8 l min⁻¹ air/0.1 l min⁻¹ O₂ (Attene vet), 5% to induce anaesthesia and 1–2.5% to sustain anaesthesia. During magnetic resonance scanning of the animals, anaesthesia was maintained at 1–1.5% isoflurane in a 1:1 mixture of air:O₂. The body temperature of the anesthetized rats was maintained at 37 °C by a homeothermic monitoring system (Harvard

Apparatus). Mechanical ventilation was included for anesthetic protocols longer than 30 min to ensure stable respiratory partial pressure of carbon dioxide and arterial oxygen saturation and thus stable plasma pH and electrolyte content. A surgical tracheotomy was performed and the ventilation controlled by the VentElite system (Harvard Apparatus) by 0.9 l min⁻¹ humidified air mixed with 0.1 l min⁻¹ O₂ adjusted with approximately 3 ml per breath, 80 breath min⁻¹, a Positive End-Expiratory Pressure (PEEP) at 2 cm, and 10% sigh for a ~400 g rat. The ventilation settings were optimized for each animal using a capnograph (Type 340, Harvard Apparatus) and a pulse oximeter (MouseOx[®] Plus, Starr Life Sciences) after system calibration with respiratory pCO₂ (4.5–5 kPa), pO₂ (13.3–17.3 kPa), and arterial oxygen saturation (98.8–99.4%) (ABL90, Radiometer). For survival procedures, the rats were preoperatively given the analgesics buprenorphine p.o. (0.4 mg kg⁻¹, Sandoz) and carprofen subcutaneously (5 mg kg⁻¹, Norbrook). The former was re-administered 24 h postoperatively.

Solutions and chemicals

The majority of the experiments were conducted in HCO₃⁻-containing artificial cerebrospinal fluid (aCSF; (in mM) 120 NaCl, 2.5 KCl, 2.5 CaCl₂, 1.3 MgSO₄, 1 NaH₂PO₄, 10 glucose, 25 NaHCO₃, pH adjusted with 95% O₂/5% CO₂). In experiments where the solution could not be equilibrated with 95% O₂/5% CO₂ during the experimental procedure (intracranial pressure monitoring and RNA sequencing), the solution was instead buffered by HEPES (HEPES-aCSF; (in mM) 120 NaCl, 2.5 KCl, 2.5 CaCl₂, 1.3 MgSO₄, 1 NaH₂PO₄, 10 glucose, 17 Na-HEPES, adjusted to pH 7.4 with NaOH). Pharmacological inhibitors were dissolved in DMSO and kept as stock solutions at –20 °C. These were either purchased from Sigma (bumetanide: B3023, GSK1016790A: G0798, RN-1734: R0658, lysophosphatidic acid: L7260, Cloxantel: 34093) or MedChemExpress (WNK463: HY-100,828). All control solutions contained appropriate concentrations of vehicle (DMSO, D8418, Sigma), which amounted to 0.05–0.1% DMSO.

Experimental intraventricular hemorrhage (IVH) in rats

The surgery was performed on rats anesthetized with isoflurane under aseptic conditions with body temperature maintained at 37 °C using a rectal probe and feedback-controlled heating pad (Harvard Apparatus). Rats were positioned in a stereotaxic frame (Harvard Apparatus) and the skull exposed with a midline incision. A cranial burr hole was drilled above the right lateral ventricle (0.6 mm posterior and 1.6 mm lateral to bregma), after which the rats were removed from the stereotaxic frame, the femoral artery catheterized, and approximately 300 µl

blood was collected (the control rats underwent sham operation). Immediately thereafter, 200 μ l of this autologous blood sample (or saline) was manually injected over the course of 15 min via a 27-gauge needle inserted stereotaxically into the burr hole in the right lateral ventricle (4.5 mm ventral) [29] and expected to spread throughout the ventricular system containing approximately 180 μ l CSF in rats of the chosen species and age ($181 \pm 18 \mu$ l, $n = 3$, quantified by MRI, see below). The needle was kept in place for 5 min before retraction to prevent backflow. The skin incisions were closed with sutures and the rats were allowed to recover before returning to the housing facility.

CSF extraction and alpha-LISA

24 h post-IVH surgery, the rats were anesthetized and placed in a stereotaxic frame. CSF was sampled from cisterna magna with a glass capillary (30-0067, Harvard Apparatus pulled by a Brown Micropipette puller, Model P-97, Sutter Instruments) placed at a 5° angle (7.5 mm distal to the occipital bone and 1.5 mm lateral to the muscle-midline). CSF was collected in polypropylene tubes (Sarstedt), centrifuged at $2000 \times g$ for 10 min at 4 °C, divided into aliquots, and stored at -80 °C. The animals were excluded from the study if blood was detected in the CSF obtained from the saline control animals (occurred in one rat). The LPA content of the CSF samples was determined with alpha-LISA by use of a ready-to-use microwell kit designed to detect native LPA in either rats (MBS774994, MyBioSource) or humans (MBS707296, MyBioSource). The CSF samples were added to wells pre-coated with LPA antibody, followed by addition of streptavidin-horseradish peroxidase to form an immune complex. Upon a wash step, chromogen substrate solutions were added and plate reading conducted in a microplate photometer (Synergy™ Neo2 Multi-mode Microplate Reader; BioTek Instruments) according to the manufacturer's instructions.

Determination of brain water content following intraventricular LPA exposure

25 μ l LPA (100 μ M) was delivered intraventricularly into anesthetized rats (sham operated rats were used as comparison) as described for the blood delivery in the IVH procedure. This concentration was chosen based on the expected (97%) loss of LPA following lipid interactions with pipettes, tubes and syringe surfaces in the absence of a lipid-carrier protein [16]. In addition, a single bolus injection into one lateral ventricle will be diluted in the entire ventricular system (of around 180 μ l) and gradually washed away from the choroid plexus surface by the sustained CSF secretion in the 24 h interval between injection and experiment. We thereby expect a substantially

lower LPA concentration at the surface of the choroid plexus over the 24 h period. 24 h post-injection, the rat was sacrificed and its brain swiftly removed, placed in a pre-weighed porcelain evaporating beaker (Witeg) and weighed within 1 min after brain isolation. The brain tissue was homogenized with a steel pestle and dried at 100 °C for 72 h to a constant mass. The dry brain was weighed, and the brain water content determined in ml/gram dry weight using the equation: (wet weight - dry weight)/dry weight. The weighing was done in a randomized and blinded fashion.

Magnetic resonance imaging (MRI)

Anesthetized rats underwent MRI in a 9.4 Tesla preclinical horizontal bore scanner (BioSpec 94/30 USR, Bruker BioSpin) equipped with a 240 mT/m gradient coil (BGA-12 S, Bruker) at the Preclinical MRI Core Facility, University of Copenhagen. The scanner was interfaced to a Bruker Avance III console and controlled by Paravision 6.1 software (Bruker). Imaging was performed with an 86 mm-inner-diameter volume resonator and a 4-channel surface quadrature array receiver coil. The animal body temperature was maintained at 37 ± 0.5 °C with a thermostatically controlled waterbed and its respiratory rate monitored by an MR-compatible monitoring system (SA Instruments). The imaging protocol consisted of T₂-weighted 2D rapid acquisition with relaxation enhancement (2D-RARE) for reference spatial planning with the following settings: repetition time (TR)=4000 ms, effective echo time (TE)=60 ms, number of averaging (NA)=4, RareFactor=4, slice thickness=500 μ m, in-plane resolution=137 \times 273 μ m, 25 coronal slices, total acquisition time (TA)=8.5 min. For obtaining high resolution CSF volumetry, a 3D constructive interference steady-state sequence (3D-CISS) [30] image was calculated as a maximum intensity projection (MIP) from 4 realigned 3D-TrueFISP volumes with 4 orthogonal phase encoding directions (TR=4.6 ms, TE=2.3 ms, NA=1, Repetitions=2, Flip angle=50°, 3D spatial resolution 100 \times 100 \times 100 μ m, RF phase advance 0, 180, 90, 270°, TA=28 min). To obtain optimal spatial uniformity, all acquired 3D-TrueFISP volumes were motion-corrected before calculation as MIP, and the image bias field was removed with Advanced Normalization Tools (ANTs) [31, 32]. For each brain sample, the total brain volume was automatically segmented by using region growing with ITK-snap (version 3.8.0) [33]. In addition, the pixel intensity factorized semi-automatic thresholding was performed to segment the lateral ventricle in each hemisphere. The volume measurement of the whole brain and lateral ventricles were performed in ITK-snap. The analysis was carried out in a blinded fashion.

ICP monitoring

A burr hole was drilled above the right lateral ventricle (using the coordinates 1.3 mm posterior to Bregma, 1.8 mm lateral to the midline, and 0.6 mm ventral through the skull) of anesthetized and ventilated rats placed in a stereotaxic frame, in which a 4 mm brain infusion cannula (Brain infusion kit 2, Alzet) was placed. On the contralateral side of the skull, an epidural probe (PlasticsOne, C313G) was placed in a cranial window (4 mm diameter) and secured with dental resin cement (Panavia SA Cement, Kuraray Noritake Dental Inc.). The cannula was pre-filled with HEPES-aCSF and connected to a pressure transducer (APT300) and a transducer amplifier module TAM-A (Hugo Sachs Elektronik). The pressure signal was visualized and recorded with a sample rate of 1 kHz using BDAS Basic Data Acquisition Software (Harvard Apparatus, Hugo Sachs Elektronik). Jugular compression was applied in the beginning and at the end of the experiment to confirm proper ICP recording. Pre-heated aCSF (containing DMSO or 1.8 mM RN1734; expected ventricular concentration 50 μM) was slowly infused ($0.5 \mu\text{l min}^{-1}$) into the lateral ventricle.

CSF production rate

The CSF production rate was determined with the ventriculo-cisternal perfusion (VCP) technique. An infusion cannula (Brain infusion kit 2, Alzet) was stereotaxically placed in the right lateral ventricle of an anesthetized and ventilated rat (using the same coordinates as for ICP), through which a pre-heated (37°C , SF-28, Warner Instruments) dextran-containing solution (HCO_3^- -aCSF containing 1 mg ml^{-1} TRITC-dextran (tetramethylrhodamine isothiocyanate-dextran, $\text{MW}=155 \text{ kDa}$; T1287, Sigma) was perfused at $9 \mu\text{l min}^{-1}$. CSF was sampled at 5 min intervals from cisterna magna as described above for CSF extraction. The cisterna magna puncture and associated continuous fluid sampling prevents elevation of the ICP during the procedure. The dilution of the infused solution is assigned to endogenously secreted CSF, irrespective of origin of this fluid [20]. 60 min into the experiment, the control test solution was replaced with one containing either TRPV4 activator (GSK, 500 nM) or TRPV4 inhibitor (RN1734, 50 μM), with an expected 2-fold ventricular dilution (more in the contralateral ventricle) followed by continuous 'wash-away' from the choroid plexus surface by the sustained CSF secretion. Continuous (24 h) exposure to high concentrations of GSK have been reported to be toxic to cultured cells [34], and we therefore verified cell viability and morphological integrity of acutely excised choroid plexus exposed to 500 nM GSK for the 1 h that mimics the VCP experimental procedure (Additional file 1: B). The

fluorescent content was measured in a microplate photometer (545 nm, Synergy™ Neo2 Multi-mode Microplate Reader; BioTek Instruments), and the production rate of CSF was calculated from the equation:

$$V_p = r_i * \frac{C_i - C_o}{C_o}$$

where V_p = CSF production rate ($\mu\text{l min}^{-1}$), r_i = infusion rate ($\mu\text{l min}^{-1}$), C_i = fluorescence of inflow solution, C_o = fluorescence of outflow solution, calculated based on stable time intervals from 50 to 65 min and 100–120 min.

Live imaging of CSF movement

Through a burr hole in the skull of the anaesthetized rat (same coordinates as for ICP and VCP), a Hamilton syringe (RN 0.40, G27, a20, AgnTho's) was placed (4 mm deep) with $15 \mu\text{l HCO}_3^-$ -aCSF containing vehicle (DMSO) or drug of interest (TRPV4 activator, 1 μM GSK; TRPV4 inhibitor, 100 μM RN1734, expected to be immediately diluted in $\sim 180 \mu\text{l}$ native CSF). The content was injected during 10 s to target both lateral ventricles. This first injection was intended to allow the inhibitors to act on their target transporters prior to introduction of the fluorescent dye. The procedure was repeated 5 min later with identical syringe content, but with addition of the carboxylate dye ($\text{MW}=1,091$, IRDye 800 CW, P/N 929-08972, LI-COR Biosciences) to the syringe content (10 μM of carboxylate dye). The rat was swiftly placed in a Pearl Trilogy Small Animal Imaging System (LI-COR Biosciences) and within 1 min after last ventricular injection, images were obtained at 30 s intervals (800 nm channel, 85 μm resolution, for 5 min). A white field image was taken at the termination of each experiment, after which the rat was sacrificed. The isolated brain was split into the two hemispheres and placed on a coverslip to record a final micrograph to ensure proper targeting of the ventricular compartment (800 nm channel). Images were analysed using LI-COR Image Studio 5.2 (LI-COR Biosciences) and data presented as fluorescence intensity in a region of interest placed in line with lambda, normalized to signals in the first image. Analyses were done in a randomized and blinded fashion.

RNASeq of rat choroid plexus

Isolated rat choroid plexus (lateral and 4th) were stored in RNAlater (R0901, Sigma) at -80°C prior to RNA extraction and library preparation (performed by Novogene Company Limited with NEB Next® Ultra™ RNA Library Prep Kit (NEB)) prior to RNA sequencing (paired-end 150 bp, with 12 Gb output) on an Illumina NovaSeq 6000 (Illumina). Quality control and adapter removal was done with Novogene. The 150 base paired-end reads

were mapped to rat reference genome Rnor_6.0.103 (*Rattus norvegicus*) using Spliced Transcripts Alignment to a Reference (STAR) RNA-seq aligner (v.2.7.2a) [35]. The mapped alignment generated by STAR was normalized to transcripts per million (TPM) [36] with RSEM (v 1.3.3) [37]. The RNAseq data obtained from this choroid plexus tissue has also been employed for other analysis [38]. Gene information was gathered with mygene 3.1.0 python library [39, 40] (<http://mygene.info>) where GO terms [41–43] for cellular components were extracted. The list of genes annotated as “Voltage-gated ion channels”, “Ligand-gated ion channels”, and “Other Ion channel” was obtained from the Guide to Pharmacology webpage (<https://www.guidetopharmacology.org/download.jsp>) [44] and employed to generate a list of plasma membrane ion channel proteins (in which ion channels in intracellular membranes were excluded). The list of rat kinases was obtained from the Kyoto Encyclopedia of Genes and Genomes (KEGG) database (<https://www.kegg.jp/kegg/genes.html>) [45], with organism specific filtering “rno” (*Rattus norvegicus*), for entries of ‘EC 2.7.10.2’ (non-specific protein-tyrosine kinase), ‘EC 2.7.12’ (Dual-specificity kinases) with the two sub-categories, and ‘EC 2.7.11’ (Protein-serine/threonine kinases) with the 33 sub-categories. Scripts and program parameters can be found at <https://github.com/Sorennorge/MacAulayLab-RNAseq1>. Network analysis was carried out with the string database (string-db.org) [46] with the search criteria: Multiple proteins in organism ‘*Rattus norvegicus*’: TRPV4, SLC12A2 (NKCC1), WNK1, WNK3, WNK4, Stk39 (SPAK).

Tissue preparation and immunohistochemistry

Anesthetized rats were perfusion fixed with 4% paraformaldehyde and the brains removed for post-fixation in the same fixative overnight, cryoprotected in 25% sucrose, and frozen on solid CO₂. Sagittal and coronal sections (16 μm) were cut and stored at –20 °C. Blockage was done with 10% swine serum diluted in PBS + 1% Tween-20 (PBST), and the sections were immunolabeled with primary rabbit anti-NKCC1 (Abcam #AB59791, 1:400) and mouse anti-TRPV4 (BD Biosciences #AB53079, 1:500) overnight at 4 °C, and Alexa FluorTM488 and Alexa FluorTM647 (ThermoFisher Scientific 1:500) for 2 h at room temperature. Finally, the sections were mounted with ProLong Gold DAPI mounting medium (Dako). The confocal images were acquired with a Zeiss LSM710 point laser (Argon Lasos RMC781272) scanning confocal microscope with a Zeiss Plan-Apochromat 63×/numerical aperture (NA) 1.4 oil objective (Carl Zeiss, Oberkochen). All micrographs were sampled in a frame scan mode.

Proximity ligation assay

Proximity ligation assay (PLA) by indirect detection was done using Duolink reagents and instructions (Sigma-Aldrich) on rat brain cryosections (16 μm) (see ‘Tissue preparation’ section). After incubation in Duolink blocking solution, the tissue sections were incubated with anti-TRPV4 (LS-Bio #LS-C94498, 1:400) and anti-NKCC1 (Dundee University #S022D, 2 μg/ml) overnight at 4 °C. The secondary antibodies were conjugated to a MINUS and a PLUS PLA probe, and were detectable as fluorescent speckles only upon close contact [47]. A technical control omitting both of the primary antibodies was included. Ligation and amplification of the samples were done according to the Duolink protocol, the sections were mounted with coverslips using the Duolink In Situ Mounting Medium with DAPI (Sigma-Aldrich). Micrographs were acquired with a Zeiss LSM700 point laser (Argon Lasos RMC781272) scanning confocal microscope with a Zeiss Plan-Apochromat 20×/numerical aperture (NA) 1.6 oil objective (Carl Zeiss, Oberkochen). All micrographs were sampled in a frame scan mode.

⁸⁶Rb⁺ efflux experiments

Acutely isolated lateral choroid plexuses were placed in cold HCO₃⁻-aCSF but allowed to recover at 37 °C for 5–10 min before the experiment. Choroidal isotope accumulation was performed by a 10 min incubation in gas-equilibrated HCO₃⁻-aCSF with 1 μCi ml⁻¹ ⁸⁶Rb⁺ (NEZ07200, Polatom) and 4 μCi ml⁻¹ ³H-mannitol (NET101, extracellular marker, PerkinElmer). The choroid plexus was briefly washed (15 s) prior to incubation in 0.5 ml efflux medium (HCO₃⁻-aCSF containing the indicated modulators; 20 μM bumetanide (NKCC1 inhibitor), 100 nM GSK (TRPV4 agonist), 50 μM RN (TRPV4 inhibitor), 20 μM Closantel (SPAK kinase-inhibitor), 20 nM WNK463 (WNK kinase-inhibitor), 25 μM LPA, or vehicle (DMSO)). 0.2 ml of the efflux medium was collected into scintillation vials at 10 s time intervals and replaced with fresh HCO₃⁻-aCSF. Upon termination of the experiment, the choroid plexuses were dissolved in 1 ml Solvable (6NE9100, PerkinElmer) and the isotope content determined by liquid scintillation counting with Ultima GoldTM XR scintillation liquid (6,013,119, PerkinElmer) in a Tri-Carb 2900TR Liquid Scintillation Analyzer (Packard). The choroid plexus ⁸⁶Rb⁺ content corrected for ³H-mannitol content (extracellular background) was calculated for each time point, and the natural logarithm of the choroid plexus content A_t/A_0 was plotted against time. Slopes indicating the ⁸⁶Rb⁺ efflux rate constants (min⁻¹) were determined from linear regression analysis [20, 48].

Electrophysiological recordings in heterologously expressing *Xenopus laevis* oocytes

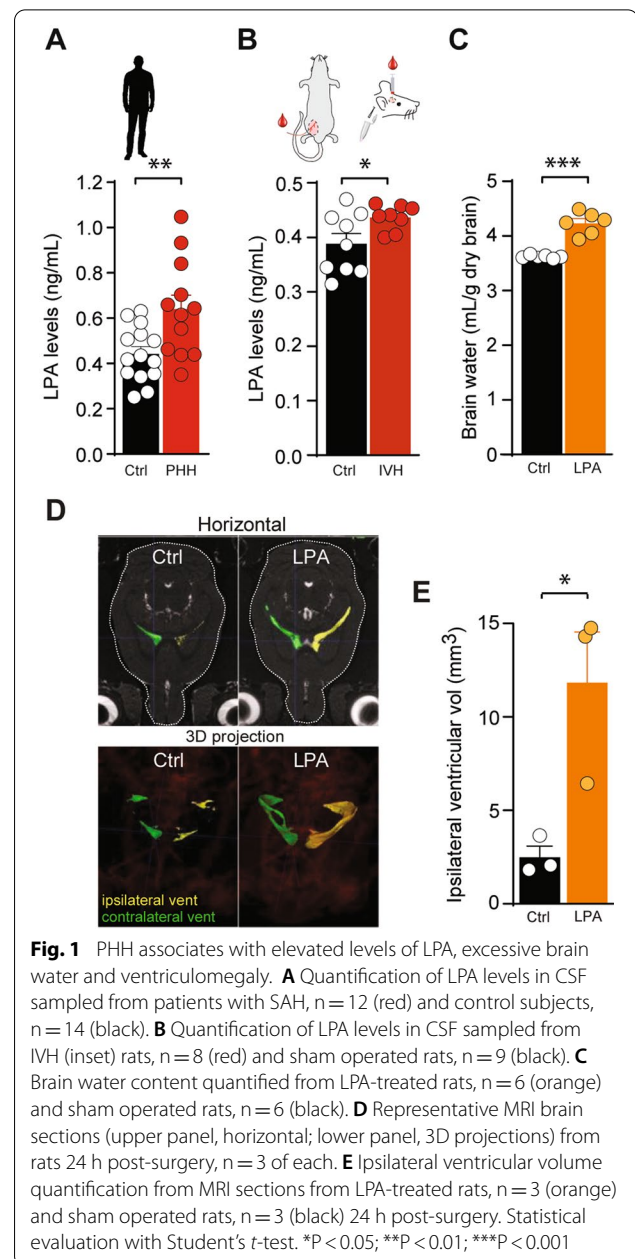
Defolliculated oocytes obtained from *Xenopus laevis* were purchased from Ecocyte Bioscience. cRNA (TRPV4) was prepared from linearized plasmids (pXOOM containing cDNA encoding TRPV4) using the mMESSAGE mMACHINE T7 kit (Ambion) and extracted with MEGAclean (Ambion), according to the manufacturer's instructions. The oocytes were microinjected with 4 ng cRNA per oocyte with a Nanoject microinjector (Drummond Scientific Company). The oocytes were kept at 19 °C for 3 days in Kulori medium prior to experiments. Oocytes were kept in Kulori medium (90 mM NaCl, 1 mM KCl, 1 mM CaCl₂, 1 mM MgCl₂, 5 mM HEPES (pH 7.4)) with inclusion of ruthenium red until the day of experiments (100 μm; Sigma Aldrich, R-2751) to suppress TRPV4 activity and ensuing cell death [49]. Conventional two-electrode voltage-clamp was performed using a DAGAN CA-1B High Performance oocyte clamp (DAGAN, Minneapolis, MN, USA) with a Digidata 1440 A interface controlled by pCLAMP software, version 10.5 (Molecular Devices, Burlingame, CA, USA). Borosilicate glass capillaries were used to pull electrodes (PIP5; HEKA Elektronik, Lambrecht, Germany) with a resistance of 1.5–3 MΩ when filled with 1 M KCl. Oocytes were placed in an experimental recording chamber and perfused with a test solution containing 100 mM NaCl, 2 mM KCl, 1 mM MgCl₂, 1 mM CaCl₂ and 10 mM HEPES (Tris buffered pH 7.4, 213 mosmol l⁻¹). Current traces were obtained by stepping the holding potential of -20 mV to test potentials ranging from -130 mV to +50 mV in increments of 15 mV in pulses of 200 msec. Recordings were low pass-filtered at 500 Hz, sampled at 1 kHz and the steady-state current activity was analysed at 160–180 ms after applying the test pulse.

Results

LPA is elevated in PHH patients

CSF from patients with PHH arising secondarily to SAH was analysed for LPA content with a sensitive alpha-LISA assay, which allows for precise detection of solutes in small fluid quantities [50]. The LPA concentration was significantly increased in the CSF from patients with SAH (0.61 ± 0.06 ng ml⁻¹, n=12) compared to CSF obtained from control subjects during preventive surgery for unruptured aneurysms (0.44 ± 0.03 ng ml⁻¹, n=14, $P < 0.05$, Fig. 1A).

No positive correlation was found between the time from ictus to sampling and CSF LPA concentration ($R^2 = 0.03$; $P = 0.57$, Additional file 1: A).



The clinical observation of elevated levels of LPA in patients with SAH is mimicked in an experimental model of intraventricular hemorrhage

To obtain an animal model of PHH with which to resolve the molecular coupling between the hemorrhagic event and hydrocephalus formation, we verified the LPA elevation observed in PHH patients in a rat model of IVH. CSF was extracted from anesthetized rats 24 h after intraventricular injection of autologous blood or sham operated and saline-injected control rats [50], Fig. 1B, and the LPA abundance was determined.

The increased LPA concentration mimicked that observed in PHH patients, as it was significantly increased in the CSF from rats with intraventricular blood delivery (0.44 ± 0.01 ng ml⁻¹, n=8) compared to that obtained from sham operated rats (0.39 ± 0.02 ng ml⁻¹, n=9, $P < 0.05$, Fig. 1B). This finding suggests that LPA elevation associates with hemorrhagic events and supports the use of an animal model of IVH to resolve potential molecular mechanisms underlying PHH.

Intraventricular LPA administration increases the brain water content and leads to ventriculomegaly

To resolve if an LPA elevation could lead to elevated brain water content, we delivered LPA directly into the lateral ventricle of anaesthetized rats and determined the brain water content 24 h after LPA administration. The total brain water content was elevated in these rats (4.23 ± 0.08 ml H₂O g⁻¹ dry brain, n=6) compared to that obtained in control rats injected with vehicle (3.62 ± 0.01 ml H₂O g⁻¹ dry brain, n=6, $P < 0.001$, Fig. 1C). To determine the distribution of the LPA-mediated excess brain fluid, the rats underwent magnetic resonance (MR) scanning 24 h post-LPA administration, and the scans demonstrated ventriculomegaly in the rats exposed to LPA (Fig. 1D and Additional file 1: C). Quantification of the volume of the ipsilateral ventricles revealed a robust enlargement in the LPA-treated animals (11.8 ± 2.7 mm³, n=3) compared to the control rats (2.6 ± 0.5 mm³, n=3, $P < 0.05$, Fig. 1E). These results indicate that LPA may directly contribute to fluid accumulation within the ventricular system of the rat brain.

LPA is a novel agonist of TRPV4, which is highly expressed in choroid plexus

To resolve the molecular link between LPA and brain water accumulation, we determined the ability of LPA to act as an agonist of the ion channel TRPV4, the activity of which is modulated by lipids [25] and which may be implicated in hydrocephalus formation [28]. To obtain an isolated setting in which to resolve LPA-mediated TRPV4 activation in the absence of other potentially LPA-sensitive ion channels or endogenous LPA receptors expressed in the choroid plexus epithelium [51], TRPV4 was heterologously expressed in *Xenopus laevis* oocytes, which allow for overexpression of the channel of interest with low endogenous background channel activity. TRPV4 current activity was monitored with conventional two-electrode voltage clamp, which demonstrated an LPA-mediated ~3-fold increase in membrane currents in TRPV4-expressing oocytes (compare 2.2 ± 0.3 μA, n=8 in LPA-treated oocytes to 0.7 ± 0.1 μA non-treated oocytes, n=9, $P < 0.01$ Fig. 2A–C). The LPA-induced

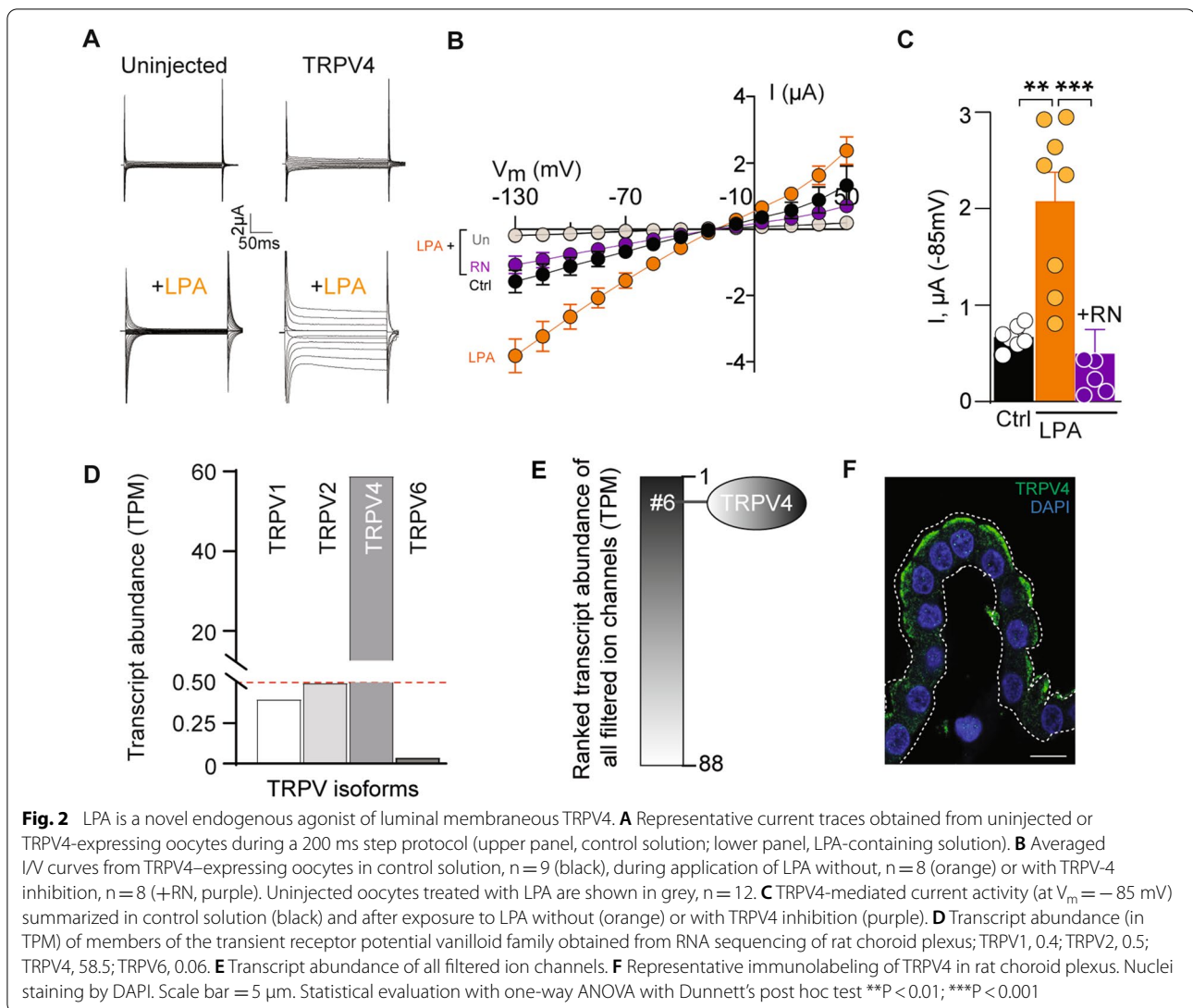
increase in TRPV4-mediated current was abolished upon inhibition of TRPV4 with the specific TRPV4 inhibitor RN1734 (RN) [52] (0.5 ± 0.3 μA, n=8, $P < 0.001$, Fig. 2C), demonstrating TRPV4 as the mediator of the LPA-induced membrane currents. The membrane currents of uninjected control oocytes were unaffected by LPA exposure (n=12, Fig. 2A, B). These data demonstrate that LPA acts as an agonist of TRPV4 and causes channel opening by its direct action on the channel. RNAseq analysis of rat choroid plexus revealed that TRPV4 is the only member of the vanilloid family of TRP channels expressed in this tissue at significant levels (>0.5 TPM; Fig. 2D). Among a filtered list of transcripts encoding ion channels expressed in choroid plexus, TRPV4 appeared as the 6th highest-expressed ion channel (Fig. 2E), and localizes to the luminal membrane of rat choroid plexus, as illustrated with immunohistochemistry (Fig. 2F).

Inhibition of TRPV4 lowers the intracranial pressure

TRPV4 inhibition alleviates ventriculomegaly in a genetic model of hydrocephalus [28]. Thus, TRPV4 may well directly influence the brain water balance and modulate the ICP. We therefore monitored the ICP in anesthetized and ventilated rats during modulation of TRPV4 channel activity. ICP dynamics were recorded with a pressure probe placed in a cranial window above dura, with a continuous slow (0.5 μl min⁻¹) infusion of artificial CSF (aCSF) (containing vehicle) into one lateral ventricle (see Fig. 3A for a schematic of the experimental setup). The ICP at the start of the experiment was 4.8 ± 0.2 mmHg, n=10 (Fig. 3B inset) and reduced slightly over the course of the experiment upon mock solution change (Fig. 3B) by $7 \pm 1\%$, n=5, Fig. 3C). Replacement of the control solution with a solution containing the TRPV4 inhibitor RN, significantly reduced the ICP ($27 \pm 2\%$, n=5) compared to that obtained in control solution ($P < 0.001$, Fig. 3B, C). These results demonstrate that TRPV4 inhibition lowers the ICP in rats in vivo and thus suggest a direct involvement of the ion channel in controlling brain fluid accumulation.

TRPV4 activity modulates the CSF production

To resolve whether the TRPV4-mediated ICP modulation originated from altered CSF production, we determined the effect of TRPV4 activity on the rate of CSF secretion in anesthetized and ventilated rats. CSF secretion was quantified by the ventriculo-cisternal perfusion (VCP) technique in which dextran-containing aCSF is perfused at a constant rate into the lateral ventricle and CSF samples collected from the cisterna magna (see Fig. 3D for a schematic). To obtain a time control experiment demonstrating the stability of the recording, the control aCSF was replaced by an identical solution after



which the CSF secretion rate remained stable during the entire experimental window ($95 \pm 3\%$ of control, $n = 7$, $P = 0.14$, Fig. 3E–G). Dextran of this size (MW 155 kDa) is cell membrane impermeable and remains within the rat ventricular system during the described procedure [22], so the CSF secretion rate is obtained by quantification of the dextran dilution that occurs upon mixing with newly secreted CSF ($7.1 \pm 0.7 \mu\text{l min}^{-1}$, $n = 7$, Fig. 3E, inset). Inhibition of TRPV4 by inclusion of the TRPV4 inhibitor RN to the infused aCSF led to a reduction in the CSF secretion rate to $75 \pm 2\%$ of control ($n = 6$, $P < 0.01$) whereas activation of TRPV4 with its agonist GSK1016790A (GSK) caused an elevation of the CSF secretion (to $113 \pm 6\%$ of control, $n = 6$, $P < 0.05$), Fig. 3F, G. These data illustrate that modulation of the TRPV4 activity affects the rate of CSF secretion in anesthetized rats. With the long experimental duration of the VCP

experiments, extrachoroidal TRPV4 could be affected and indirectly modulate CSF secretion e.g. via change in cardiovascular parameters and nerve activity. To obtain a swifter, and less invasive, protocol for determining the rate of CSF secretion, we employed whole animal live imaging of CSF dynamics based on a fluorescent tracer. A fluorescent dye (IRDye 800CW) was injected into the lateral ventricle of an anesthetized rat (see example of correctly targeted dye delivery in Fig. 3H), which was immediately placed in the fluorescent scanner. Recording of the caudal redistribution of the fluorescent dye initiated within 1 min of dye injection served as a proxy of CSF production. The dye movement is seen as superimposed pseudo-color fluorescence (Fig. 3I, J) and the dye intensity quantified in a region of interest placed in line with lambda (Fig. 3I). Intraventricular delivery of the

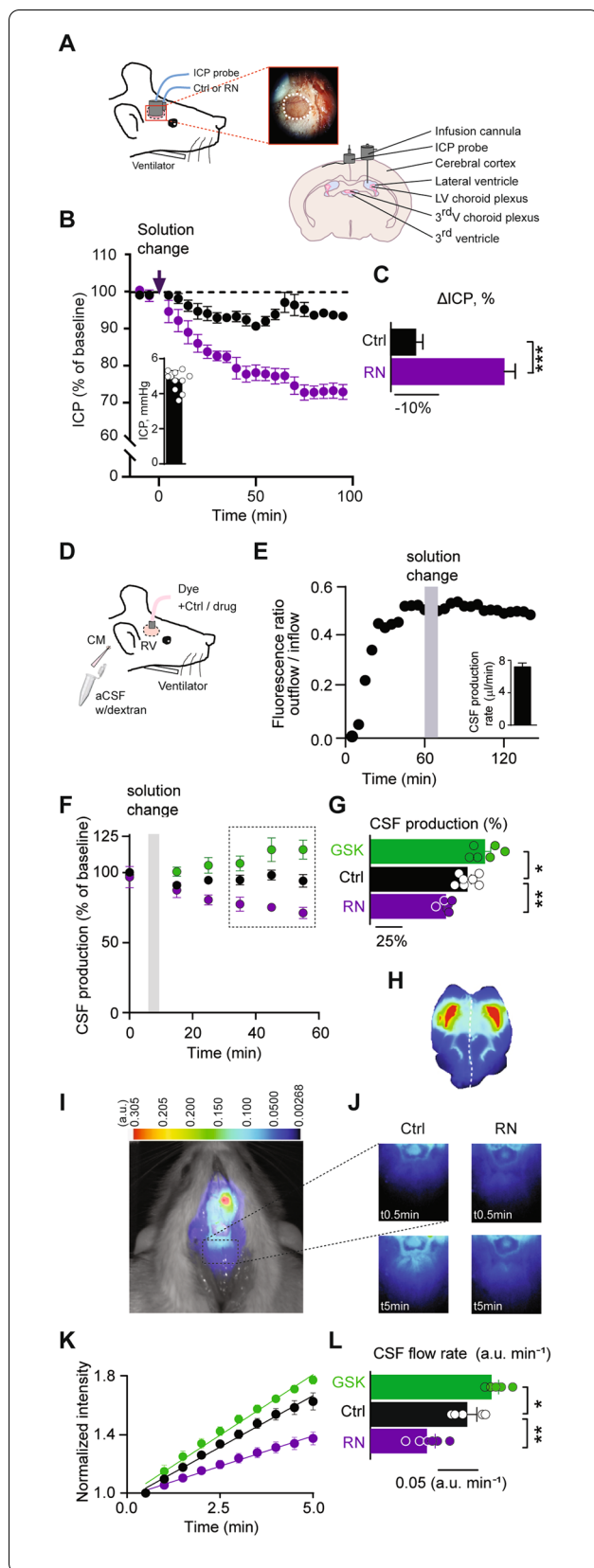
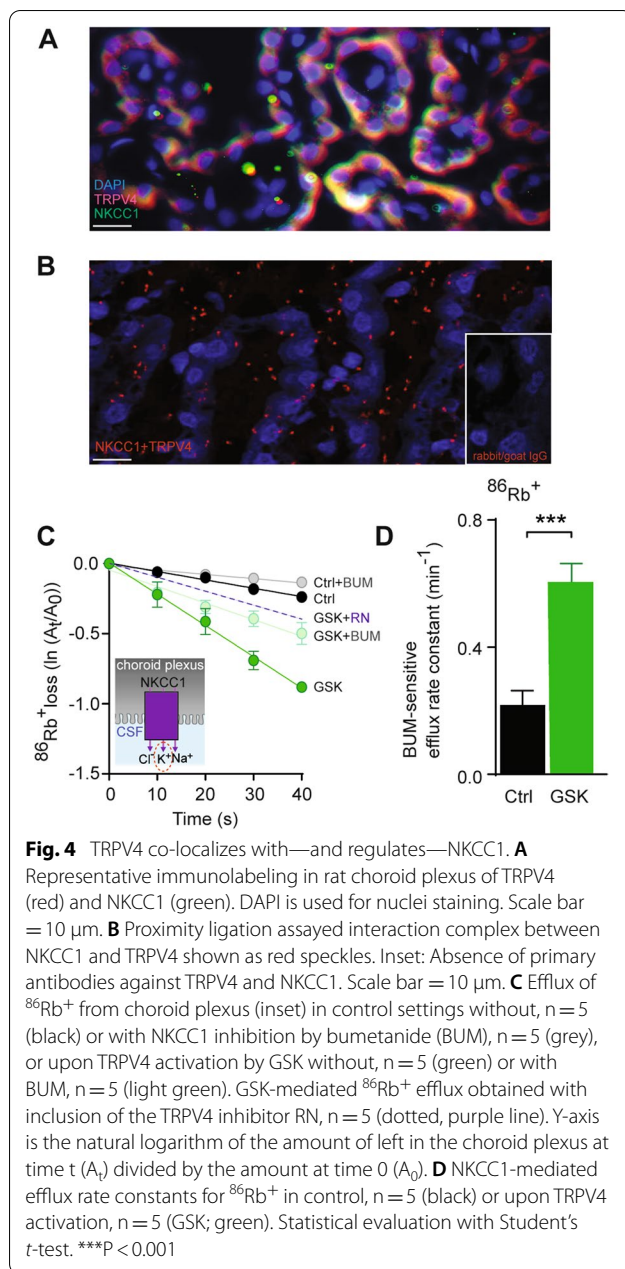


Fig. 3 TRPV4 activity modulates ICP and CSF production in vivo. **A** Schematic illustrating the cranial window (shown as a dotted circle) into which the ICP probe is positioned, LV; lateral ventricle. **B** ICP as a function of time upon infusion of control solution, $n = 5$ (black) or TRPV4 inhibitor-containing solution, $n = 5$ (RN; purple) shown as 5 min average values normalized to the baseline. Inset, initial ICP, $n = 10$. **C** Summarized changes in ICP with control solution (black) and TRPV4 inhibitor-containing solution after 1.5 h. **D** Schematic of the VCP method used to determine the CSF production rate. **E** Representative time course of the dextran ratio (outflow/inflow) with a mock solution change with control solution (indicated with a grey bar). Inset, average CSF production rate, $n = 7$. **F** CSF production as a function of time. Data normalized to the last four samples before solution change to either the control solution, $n = 7$ (black), the TRPV4 activator GSK, $n = 6$ (green), or the TRPV4 inhibitor RN, $n = 6$ (purple). **G** Summarized CSF production rates in % of control after exposure to vehicle (black), TRPV4 activation (green) and TRPV4 inhibition (purple). **H** Correctly targeted dye delivery in mid-sagittal sections of a rat brain. **I** A representative image of a rat after injection of IRDye 800CW carboxylate dye (superimposed pseudo-color). The square placed in line with lambda indicates the area of dye content quantification. **J** Representative images obtained at $t = 0.5$ ($t_{0.5}$) and $t = 5$ (t_5) min in control solution (left) or upon TRPV4 inhibition (RN; right). **K** The dye intensity normalized to that obtained in the first image and plotted as a function of time representing flow rate for control, $n = 5$ (black), TRPV4 activation, $n = 6$ (GSK, green) and TRPV4 inhibition, $n = 6$ (RN, purple). **L** Quantification of the dye intensity (flow rate) determined from linear regression in **K** over the 5 min. time window from control (black), TRPV4 activation (green) and TRPV4 inhibition (purple). Statistical evaluation with Student's t -test (**C**) or one-way ANOVA with Dunnett's post hoc test (**F** and **K**) * $P < 0.05$; ** $P < 0.01$; *** $P < 0.001$

TRPV4 inhibitor RN reduced the dye movement by 38% (from 0.13 ± 0.01 a.u. min^{-1} , $n = 5$ in control animals to 0.08 ± 0.01 a.u. min^{-1} , $n = 6$, $P < 0.01$), while inclusion of the TRPV4 agonist GSK increased the flow rate 23% (to 0.16 ± 0.01 a.u. min^{-1} , $n = 6$, $P < 0.05$), Fig. 3K, L. Taken together, these findings reveal that TRPV4 activity directly modulates the CSF secretion rate.

TRPV4 co-localizes with NKCC1 and modulates the CSF secretion apparatus by NKCC1 activation

With a polarization to the luminal membrane, TRPV4 could exert its stimulatory effect on CSF secretion by modulation of the cotransporter NKCC1 that is implicated in CSF secretion [6, 20, 21]. TRPV4 and NKCC1 both localized to the luminal membrane of choroid plexus, as demonstrated by immunohistochemistry (Fig. 4A). Their close proximity (30–40 nm) was verified with the proximity ligation assay [47], in which fluorescent speckles occur solely when the respective antibodies are in close proximity, as demonstrated in (Fig. 4B). Fluorescent speckles were absent if the primary antibodies was omitted (Fig. 4B, inset). These results indicate that TRPV4 and NKCC1 are co-localized on the luminal membrane of the choroid plexus. To reveal whether this co-localization represented a functional



interaction between TRPV4 and NKCC1, we quantified the NKCC1 transport activity with ex vivo radioisotope efflux experiments in acutely isolated rat choroid plexus pre-loaded with $^{86}\text{Rb}^+$, which serves as a congener for K^+ (Fig. 4C inset). TRPV4 activation by GSK increased the rate of $^{86}\text{Rb}^+$ efflux ~ 4 fold (from $0.35 \pm 0.06 \text{ min}^{-1}$, $n=5$, in control to $1.32 \pm 0.15 \text{ min}^{-1}$, $n=5$, $P < 0.001$, Fig. 4C). A direct effect on NKCC1-mediated efflux was ascertained with inclusion of the NKCC1 inhibitor bumetanide [53], which reduced the GSK-mediated efflux (to $0.71 \pm 0.09 \text{ min}^{-1}$, $n=5$, Fig. 4C). The

molecular origin of the bumetanide-insensitive fraction of the GSK-induced $^{86}\text{Rb}^+$ efflux remains unresolved but is most likely representative of K^+ channel activity. These data thus illustrated a GSK-mediated ~ 3 fold increase in the bumetanide-sensitive part of the $^{86}\text{Rb}^+$ efflux ($0.22 \pm 0.05 \text{ min}^{-1}$ compared to $0.61 \pm 0.06 \text{ min}^{-1}$, Fig. 4D, $P < 0.001$), which is thus assigned to elevated NKCC1 activity. Verification of the TRPV4-mediated increase in the NKCC1-mediated efflux rate was obtained with attenuation of the GSK-mediated elevation of the $^{86}\text{Rb}^+$ efflux by inclusion of the TRPV4 inhibitor, RN (to $0.66 \pm 0.02 \text{ min}^{-1}$, $n=5$). These data demonstrate a robust TRPV4-mediated increase in NKCC1 activity in choroid plexus.

TRPV4-mediated Ca^{2+} influx activates NKCC1 in a WNK-SPAK-dependent manner

To reveal whether TRPV4-mediated Ca^{2+} fluctuations are permissive for the NKCC1 activation, we determined the NKCC1 activity, assessed by $^{86}\text{Rb}^+$ efflux experiments on ex vivo rat choroid plexus, in the absence of Ca^{2+} (Ca^{2+} -free test solutions and chelation of $[\text{Ca}^{2+}]_i$ with BAPTA-AM). The $^{86}\text{Rb}^+$ efflux in the presence of GSK ($1.41 \pm 0.12 \text{ min}^{-1}$, $n=4$) was reduced in the absence of Ca^{2+} ($0.78 \pm 0.07 \text{ min}^{-1}$, $n=4$, $P < 0.01$), Fig. 5A, B. The GSK-mediated $^{86}\text{Rb}^+$ efflux was thus halved in the absence of Ca^{2+} ($1.10 \pm 0.09 \text{ min}^{-1}$ compared to $0.53 \pm 0.05 \text{ min}^{-1}$, Fig. 5B), suggesting that NKCC1 is activated by TRPV4 via its ability to cause Ca^{2+} accumulation in the choroid plexus upon channel activation.

Ca^{2+} fluctuations may regulate the WNK and SPAK kinases [54], the latter of which has been implicated in NKCC1-mediated hypersecretion of CSF (Fig. 5C) [6]. RNAseq from rat choroid plexus revealed SPAK as the most abundantly expressed kinase, with WNK1 placing at rank 74, WNK2 at rank 130 and WNK4 at rank 240 out of the 297 kinases detected in the RNAseq data (Fig. 5D). Network analysis illustrates established links between NKCC1 and the kinases with a single putative connection to TRPV4 (Fig. 5E). The TRPV4/NKCC1/WNK1/4 have a high confident score (> 0.7 string score), whereas TRPV4 is only connected to the network through co-mentions in the literature with medium string score of 0.51. To determine whether TRPV4-mediated Ca^{2+} dynamics activate NKCC1 in a WNK and/or SPAK-dependent fashion, we determined GSK-mediated choroidal NKCC1 activity, by ex vivo $^{86}\text{Rb}^+$ efflux experiments, in the presence of inhibitors of these kinases. Inhibition of SPAK and WNK did not affect the basal NKCC1 activity (Fig. 5F, H), but the SPAK inhibitor closantel [6], strongly reduced the GSK-mediated $^{86}\text{Rb}^+$ efflux (from $0.81 \pm 0.04 \text{ min}^{-1}$, $n=6$ to $0.15 \pm 0.03 \text{ min}^{-1}$, $n=6$, $P < 0.001$), Fig. 5F, G.

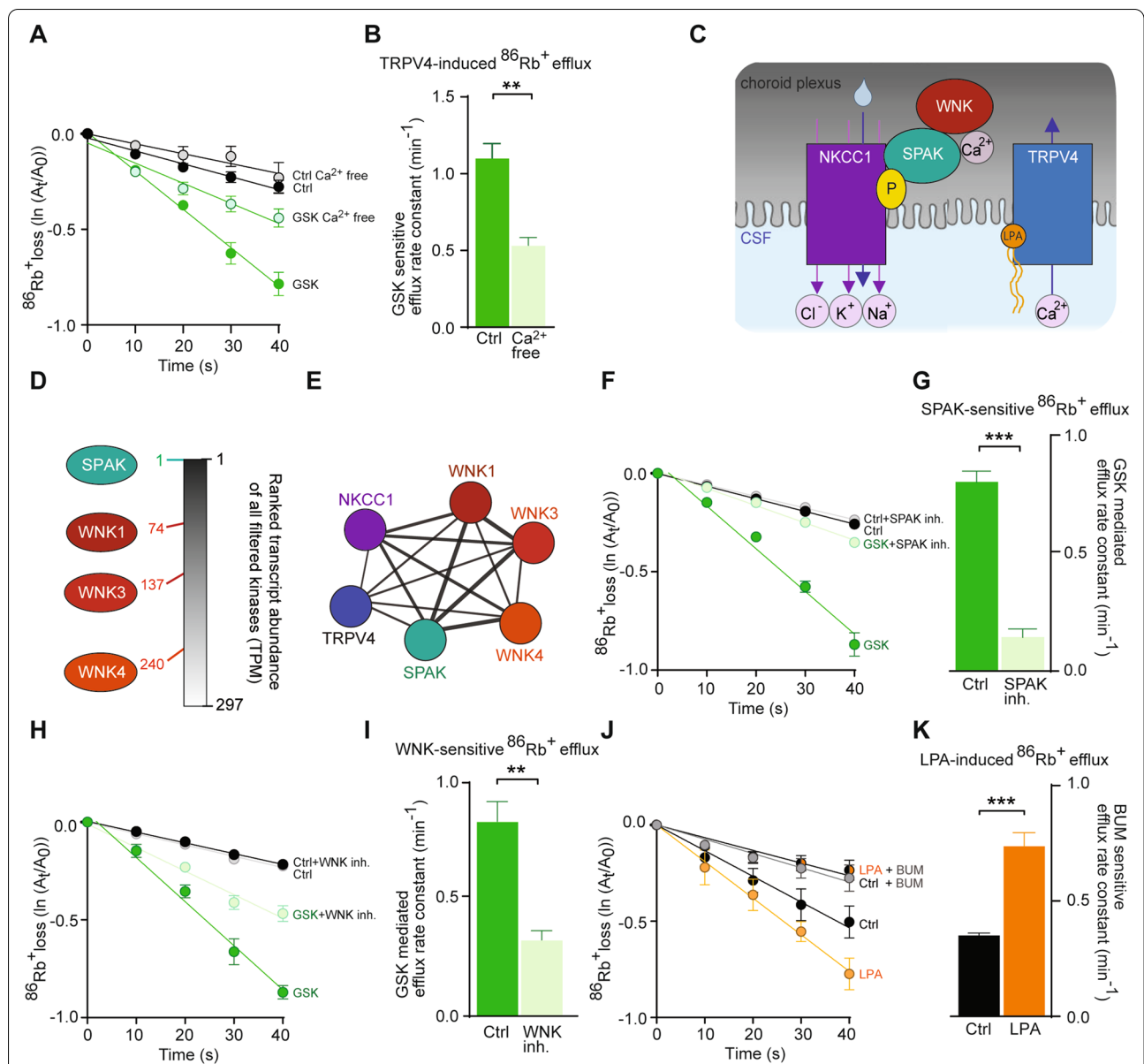


Fig. 5 TRPV4-mediated Ca^{2+} fluctuations activate NKCC1 in a WNK-SPAK-dependent manner. **A** Efflux of $^{86}\text{Rb}^{+}$ from choroid plexus in control solution, $n = 4$ (black), in Ca^{2+} -free solution, $n = 4$ (grey), upon TRPV4-activation by GSK with, $n = 4$ (green) or without Ca^{2+} , $n = 4$ (light green). **B** GSK-sensitive efflux rate constants for $^{86}\text{Rb}^{+}$ with (green) or without (light green) Ca^{2+} present. **C** Schematic of the hypothesized LPA-induced TRPV4-mediated Ca^{2+} influx regulating WNK-SPAK-mediated phosphorylation of NKCC1. **D** Transcript abundance of filtered kinases in rat choroid plexus with rank of SPAK and WNK kinases depicted. **E** Network analysis depicting published protein-protein associations amongst those illustrated in Panel A. **F** $^{86}\text{Rb}^{+}$ efflux from choroid plexus in control settings without, $n = 6$ (black) or with SPAK inhibition, $n = 6$ (grey), or upon TRPV4 activation by GSK without, $n = 6$ (green) or with, $n = 6$ (light green) SPAK inhibition. Y-axis is the natural logarithm of the amount of left in the choroid plexus at time t (A_t) divided by the amount at time 0 (A_0). **G** GSK-mediated efflux rate constants for $^{86}\text{Rb}^{+}$ without (green) or with SPAK-inhibition (light green). **H** $^{86}\text{Rb}^{+}$ efflux in control settings without, $n = 5$ (black) or with, $n = 5$ (grey) WNK inhibition, or upon TRPV4 activation by GSK without, $n = 5$ (green) or with, $n = 5$ (light green) WNK inhibition. **I** GSK-mediated efflux rate constants for $^{86}\text{Rb}^{+}$ without (green) or with (light green) WNK-inhibition. **J** $^{86}\text{Rb}^{+}$ efflux in control settings without, $n = 5$ (black) or with, $n = 5$ (grey) NKCC1 inhibition by bumetanide (BUM), or upon application of LPA without, $n = 5$ (orange) or with, $n = 5$ (black/orange) NKCC1 inhibition (BUM). **K** BUM-sensitive efflux rate constants for $^{86}\text{Rb}^{+}$ in control setting (black) or upon LPA application (orange). Statistical evaluation with Student's t -test. * $P < 0.05$; ** $P < 0.01$; *** $P < 0.001$

The pan-WNK inhibitor WNK463 [55] reduced the GSK-mediated $^{86}\text{Rb}^+$ efflux (from $0.87 \pm 0.16 \text{ min}^{-1}$, $n=5$ to $0.39 \pm 0.07 \text{ min}^{-1}$, $n=5$, $p < 0.01$), Fig. 5H, I. The GSK-mediated $^{86}\text{Rb}^+$ efflux was thus more than halved by WNK inhibition and completely abolished by SPAK inhibition. These data demonstrate that NKCC1 is activated by TRPV4 via Ca^{2+} -mediated activation of the WNK/SPAK signalling pathway.

LPA activates NKCC1 in choroid plexus

With the demonstration of LPA-mediated TRPV4 activation (Fig. 2) and TRPV4-induced NKCC1 activation (Fig. 4) promoting CSF hypersecretion (Fig. 4), we verified LPA-mediated hyperactivity of NKCC1 in choroid plexus by assessing the $^{86}\text{Rb}^+$ efflux rate in the presence of this lipid. LPA elevated the efflux rate (from $0.36 \pm 0.01 \text{ min}^{-1}$, $n=5$ to $0.74 \pm 0.05 \text{ min}^{-1}$, $n=5$, $P < 0.001$, Fig. 5J) in a bumetanide-sensitive manner, which demonstrated a ~2-fold increase in NKCC1 activity upon inclusion of LPA (Fig. 5K). LPA is thus indeed able to act in situ and mediate NKCC1 hyperactivity in choroid plexus.

Discussion

Here, we reveal a molecular coupling between a brain hemorrhagic event and the ensuing ventricular enlargement signifying PHH. The origin of hydrocephalus formation is generally sought in blockage of the CSF exit routes [56–59]. In conditions with no discernable exit route blockage, ventriculomegaly could be caused by a component of CSF hypersecretion [6, 60–63]. Hypersecretion of CSF may occur particularly in hydrocephalus etiologies where inflammation could be a pathogenetic factor [6, 60, 63]. However, here we report that the mere presence of a blood lipid, LPA, appears to contribute to the CSF hypersecretion that may lead to ventriculomegaly in experimental rats. We detected an elevation of the phospholipid LPA in the CSF from patients with SAH and from rats following experimentally-induced IVH. Such LPA elevation has previously been reported for patients and mice experiencing traumatic brain injury [15], indicative of brain entrance of the serum lipid LPA [14] along with the hemorrhagic event. Such ventricular LPA elevation is able to mimic the hemorrhagic event and cause ventriculomegaly and elevated ICP in the week(s) following intracranial LPA administration [16, 17]. These LPA-mediated morphological changes were effectuated via the G protein-coupled LPA receptors expressed in the brain tissue (LPA_{R1} - LPA_{R6}) [16–18]. Here, we demonstrate an additional acute (24 h) effect of intraventricularly-delivered LPA causing ventriculomegaly and elevated brain fluid content in adult rats by its ability to act as an agonist of the TRPV4 channel. TRPV4

is expressed in various tissues and cell types throughout the body, for review see [25], but in the brain it is highly concentrated in the choroid plexus [26, 28, 64], in which we reveal it as the 6th highest-expressed ion channel, localized to the luminal membrane (this study and [24]). Inhibition of TRPV4 modulates transepithelial ion flux in immortalized choroid plexus cell lines [26, 27] and abolishes ventriculomegaly in a genetic rat model of hydrocephalus [28]. Accordingly, we demonstrated an acute reduction of ICP in healthy rats exposed to an intraventricularly-delivered TRPV4 inhibitor. The reduction in ICP came about by TRPV4's ability to directly modulate the rate of CSF secretion. TRPV4 activity thus modulates the CSF secretion rate in healthy rats and thereby may contribute to governing of the ICP. Notably, with its luminal localization on the choroid plexus, TRPV4 inhibitors may fail to reach the target if non-cell permeable inhibitors are delivered i.p., therefore the lack of effect on CSF secretion upon inclusion of TRPV4 inhibitor in an earlier study [65].

TRPV4 can be directly activated by various lipid compounds [25], and we here add LPA to the list of lipid agonists of TRPV4. LPA exposure elevated the TRPV4-mediated current in TRPV4-expressing *Xenopus laevis* oocytes, an elevation that was absent in the presence of a TRPV4 inhibitor and in control oocytes lacking TRPV4 expression. Such a reduced experimental system allows for determination of direct functional interactions and promoted LPA as an agonist of TRPV4. The molecular coupling between TRPV4 activation and elevated activity of a transport mechanism implicated in CSF secretion originated in the TRPV4-mediated Ca^{2+} influx, which activated the WNK/SPAK signaling pathway as also observed in salivary glands [54]. These kinases are highly expressed in choroid plexus, with SPAK ranking as the highest expressed kinase (this study), and are well-established regulators of NKCC1 activity via modulation of the transporter phosphorylation status [6, 66, 67]. Activation of this pathway, with either LPA or a well-established synthetic lipid agonist of TRPV4, terminated in NKCC1 hyperactivity and a resultant elevation of the CSF secretion rate (see schematic in Fig. 5). NKCC1 is a key contributor to the CSF secretion in mice, rats, and dogs [6, 20, 21] as revealed with intraventricular delivery of the NKCC1 inhibitor bumetanide. With alternative delivery routes (i.v. or i.p.), bumetanide fails to reach its target on the luminal surface of choroid plexus in sufficient concentrations [6, 65]. A coupling between the SPAK/WNK signaling cascade and NKCC1-mediated CSF hypersecretion has previously been described in an experimental IVH rat model [6]. That study, however, promoted the immune receptor TLR4 and $\text{NF}\kappa\text{B}$ as the molecular links between the hemorrhagic event and the SPAK-induced

NKCC1-mediated CSF hypersecretion [6]. These two PHH-related molecular pathways both promoting NKCC1 hyperactivity could well occur in parallel on different time scales with the LPA/TRPV4-mediated effects discernible within minutes, followed by a slower route (perhaps minutes–hours) through a hemorrhage/TLR4-mediated path through NF κ B-mediated transcription events leading to activation of SPAK [6]. On a more prolonged time scale (days–weeks) LPA may act on its various G protein-coupled receptors and promote the ciliopathy, 3rd ventricular occlusion [16, 17], and potentially other micro-blockages not discernible on brain imaging, together contributing to the ventriculomegaly characteristic of PHH. Notably the LPA receptor expression in brain tissue is developmentally regulated [68] and it remains, at present, unresolved if the LPA-mediated pathological morphological changes observed in the neonatal mice [16, 17] would occur in the adult. PHH may thus occur by various mechanisms and in distinct structures in the brain at different time points following the hemorrhagic event [60]. Importantly, it appears that PHH arises, in part, from a component of CSF hypersecretion (this study and [6, 63]), which may well occur in other brain pathologies with disturbed brain fluid dynamics. Delineation of the molecular underpinnings governing this (and other) CSF secretory disturbances may open new avenues for the pharmacological therapy wanting for these conditions. Although more could arise with future studies, potential targets could be TRPV4 [28], the LPA signalling pathways [15], the NKCC1 [6], or the regulatory kinases, SPAK [69, 70] and the serum/glucocorticoid-regulated kinase 1 (SGK1) [71] inhibition of which may reduce hydrocephalus or lesion size in different cerebral pathological insults.

Limitations to the study include CSF sampling from cisterna magna in the rodent experimentation, from the ventricular compartment in the patients with SAH, and from the basal cisterns in the control patients. The different patient sample sites were dictated by ethical limitations in invasive CSF sampling, but could influence our results if the CSF composition differs between these locations. The control samples may contain blood contamination from the surgical opening. Such contamination is expected to raise the LPA levels in the control CSF. Our results would thus be expected to show even further differences between the two CSF groups, if one could test control CSF samples with no traces of blood. In the rat IVH model, the control rats received a saline injection (instead of the orthologous blood injection) and were therefore not naïve at the point of CSF sampling 24 h later. We cannot rule out that this manipulation could promote an inflammatory response, which in itself could affect the CSF

LPA levels. However, the human CSF samples were obtained from patients undergoing preventive surgical clipping of unruptured aneurisms and therefore had to such surgical intervention prior to the sampling event. Of note, with the invasive nature of experimental approaches towards determination of agonist-induced modulation of intracranial pressure, cerebrospinal fluid secretion rates, and choroidal transport mechanisms, these parameters were obtained from the rodent (IVH) animal model. Such findings may not fully capture the human SAH condition. With the expected lipid-plastic interaction during the experimental procedures, most (approximately 97% [16]) of the LPA is lost in the process. The concentration of free LPA in our experimental solutions is therefore an estimate and may not exactly match the concentrations detected in the CSF of humans and rats. Lastly, with the expected interplay with different transport mechanisms and regulatory factors present in the choroid plexus, our data may just reveal one segment of hemorrhage-related hydrocephalus formation. TRPV4 activation or LPA elevation may well act on other transporters or processes in the CSF secreting tissue and/or on the ventricular lining or various drainage pathways.

In conclusion, we demonstrate that the serum lipid LPA, entering the ventricular system during a hemorrhagic event, acts directly on TRPV4, and thus serves as a novel lipid agonist of this choroidal ion channel. Activation of TRPV4 causes the NKCC1 hyperactivity underlying the TRPV4-mediated elevated CSF secretion rate seemingly contributing to the ensuing ventriculomegaly signifying PHH. Future studies aimed at elucidating the pathophysiological changes in brain fluid dynamics occurring with diverse neuropathologies, ideally, should take into account formation rates of CSF, its path through the ventricular system, as well as its drainage, as most of these pathologies are likely to affect more than one of these aspects.

Supplementary Information

The online version contains supplementary material available at <https://doi.org/10.1186/s12987-022-00361-9>.

Additional file 1. LPA quantification, choroid plexus viability, and 3D imaging of the rat ventricular system.

Acknowledgements

We thank laboratory manager Trine Lind Devantier and technician Rikke Lundorff, the Core Facility for Integrated Microscopy and the Panum NMR Core Facility, Faculty of Health and Medical Sciences, University of Copenhagen.

Author contributions

Conception and design of research: TLTB and NM; Patient contact and CSF sampling: MJ, NR, MHO, NHN, TC; Conduction of the experiments: TLTB, DB, EKH, SDL, SNA, MFR; Analysis of data: TLTB, DB, EKH, SDL, SNA; Interpretation of results: TLTB and NM; Preparation of figures: TLTB; Drafting of manuscript:

TLTB and NM; Revision and approval of manuscript: TLTB, DB, EKH, SDL, SNA, NR, MHO, NHH, TC, MFR, MJ, and NM. All authors read and approved the final manuscript.

Funding

The project was funded by the Lundbeck Foundation (R303-2018-3005 to TLTB and R276-2018-403 to NM), the Weimann Foundation (to TLTB), the Novo Nordic Foundation (Tandem grant NNF17OC0024718 to NM and MJ), IMK Almene Fond (to NM), the Carlsberg Foundation (CF19-0056 to NM), Læge Sofus C.E. Friis og Hustru Olga D. Friis' scholarship (to NM) and the Research Council at Copenhagen University Hospital Rigshospitalet (E-23565-03 to TC).

Availability of data and materials

The datasets used and/or analyzed during the current study are available from the corresponding author on reasonable request.

Declarations

Ethics approval and consent to participate

Written informed consent were obtained from all patients or next of kin depending on the capacity of the patients. The patient study was approved by the Ethics committee of the Capital Region of Denmark (H-19001474 and H-17011472/69197). Animal experiments performed at University of Copenhagen conformed to the legislations for animal protection and care in the European Community Council Directive (2010/63/EU) and followed all ethical regulations under animal permission no. 2018-15-0201-01595 authorized by the Danish Animal Inspectorate. Animal experiments performed at University of Michigan were approved by the University of Michigan Committee on the Use and Care of Animals and followed the Guide for The Care and Use of Laboratory Animals (National Research Council, USA).

Consent for publication

Not applicable.

Competing interests

The authors declare that they have not competing interests.

Author details

¹Department of Neuroscience, Faculty of Health and Medical Sciences, University of Copenhagen, Blegdamsvej 3, 2200 Copenhagen, Denmark. ²Department of Neurosurgery, Neuroscience Centre, Copenhagen University Hospital - Rigshospitalet, Copenhagen, Denmark. ³Department of Neuroanaesthesiology, Neuroscience Centre, Copenhagen University Hospital - Rigshospitalet, Copenhagen, Denmark. ⁴Department of Clinical Medicine, University of Copenhagen, Copenhagen, Denmark.

Received: 8 April 2022 Accepted: 20 July 2022

Published online: 06 September 2022

References

- Spector R, Keep RF, Robert Snodgrass S, Smith QR, Johanson CE. A balanced view of choroid plexus structure and function: focus on adult humans. *Exp Neurol*. 2015;267:78–86.
- MacAulay N. Molecular mechanisms of brain water transport. *Nat Rev Neurosci*. 2021;22:326–344.
- Johanson CE, Duncan JA, Klinge PM, Brinker T, Stopa EG, Silverberg GD. Multiplicity of cerebrospinal fluid functions: new challenges in health and disease. *Cerebrospinal Fluid Res*. 2008;5:10.
- Serot JM, Zmudka J, and Jouanny P. A possible role for CSF turnover and choroid plexus in the pathogenesis of late onset Alzheimer's disease. *J Alzheimers Dis*. 2012;30:17–26.
- Hallaert GG, Vanhauwaert DJ, Logghe K, Van den Broecke C, Baert E, Van Roost D, and Caemaert J. Endoscopic coagulation of choroid plexus hyperplasia. *J Neurosurg Pediatr*. 2012;9:169–77.
- Karimy JK, Zhang J, Kurland DB, Theriault BC, Duran D, Stokum JA, Furey CG, Zhou X, Mansuri MS, Montejó J, Vera A, DiLuna ML, Delpire E, Alper SL, Gunel M, Gerzanich V, Medzhitov R, Simard JM, and Kahle KT. Inflammation-dependent cerebrospinal fluid hypersecretion by the choroid plexus epithelium in posthemorrhagic hydrocephalus. *Nat Med*. 2017;23:997–1003.
- Ducros A and Biousse V. Headache arising from idiopathic changes in CSF pressure. *Lancet Neurol*. 2015;14:655–68.
- Chen Q, Feng Z, Tan Q, Guo J, Tang J, Tan L, Feng H, Chen Z. Post-hemorrhagic hydrocephalus: recent advances and new therapeutic insights. *J Neurol Sci*. 2017;375:220–30.
- Strahle J, Garton HJ, Maher CO, Muraszko KM, Keep RF, and Xi G. Mechanisms of hydrocephalus after neonatal and adult intraventricular hemorrhage. *Transl Stroke Res*. 2012;3:25–38.
- Klebe D, McBride D, Krafft PR, Flores JJ, Tang J, and Zhang JH. Posthemorrhagic hydrocephalus development after germinal matrix hemorrhage: Established mechanisms and proposed pathways. *J Neurosci Res*. 2020;98:105–120.
- Hill A, Shackelford GD, and Volpe JJ. A potential mechanism of pathogenesis for early posthemorrhagic hydrocephalus in the premature newborn. *Pediatrics*. 1984;73:19–21.
- Mazzola CA, Choudhri AF, Auguste KI, Limbrick DD, Jr., Rogido M, Mitchell L, Flannery AM, Pediatric Hydrocephalus Systematic R, and Evidence-Based Guidelines Task F. Pediatric hydrocephalus: systematic literature review and evidence-based guidelines. Part 2: Management of posthemorrhagic hydrocephalus in premature infants. *J Neurosurg Pediatr*. 2014;14 Suppl 1:8–23.
- Shoeman D, Portess H, and Sparrow O. A review of the current treatment methods for posthaemorrhagic hydrocephalus of infants. *Cerebrospinal Fluid Res*. 2009;6:1.
- Aoki J, Taira A, Takanezawa Y, Kishi Y, Hama K, Kishimoto T, Mizuno K, Saku K, Taguchi R, and Arai H. Serum lysophosphatidic acid is produced through diverse phospholipase pathways. *J Biol Chem*. 2002;277:48737–44.
- Crack PJ, Zhang M, Morganti-Kossmann MC, Morris AJ, Wojciak JM, Fleming JK, Karve I, Wright D, Sashindranath M, Goldshmit Y, Conquest A, Daglas M, Johnston LA, Medcalf RL, Sabbadini RA, and Pebay A. Anti-lysophosphatidic acid antibodies improve traumatic brain injury outcomes. *J Neuroinflammation*. 2014;11:37.
- Lummis NC, Sanchez-Pavon P, Kennedy G, Frantz AJ, Kihara Y, Blaho VA, and Chun J. LPA1/3 overactivation induces neonatal posthemorrhagic hydrocephalus through ependymal loss and ciliary dysfunction. *Sci Adv*. 2019;5:eaax2011.
- Yung YC, Mutoh T, Lin ME, Noguchi K, Rivera RR, Choi JW, Kingsbury MA, and Chun J. Lysophosphatidic acid signaling may initiate fetal hydrocephalus. *Sci Transl Med*. 2011;3:99ra87.
- Yung YC, Stoddard NC, and Chun J. LPA receptor signaling: pharmacology, physiology, and pathophysiology. *J Lipid Res*. 2014;55:1192–214.
- Eisenberg HM, McComb JG, and Lorenzo AV. Cerebrospinal fluid overproduction and hydrocephalus associated with choroid plexus papilloma. *J Neurosurg*. 1974;40:381–5.
- Steffensen AB, Oernbo EK, Stoica A, Gerkau NJ, Barbuskaite D, Tritsarlis K, Rose CR, and MacAulay N. Cotransporter-mediated water transport underlying cerebrospinal fluid formation. *Nat Commun*. 2018;9:2167.
- Javaheri S and Wagner KR. Bumetanide decreases canine cerebrospinal fluid production. In vivo evidence for NaCl cotransport in the central nervous system. *J Clin Invest*. 1993;92:2257–61.
- Oernbo EK, Steffensen AB, Khamesi PR, Toft-Bertelsen TL, Barbuskaite D, Vilhardt F, Gerkau NJ, Tritsarlis K, Simonsen AH, Lolansen SD, Andreassen SN, Hasselbalch SG, Zeuthen T, Rose CR, Kurtcuoglu V, MacAulay N. Cerebrospinal fluid formation is controlled by membrane transporters to modulate intracranial pressure. *Fluids Barriers CNS*. 2022. <https://doi.org/10.1101/2021.12.10.472067>.
- Liedtke W, Choe Y, Marti-Renom MA, Bell AM, Denis CS, Sali A, Hudspeth AJ, Friedman JM, and Heller S. Vanilloid receptor-related osmotically activated channel (VR-OAC), a candidate vertebrate osmoreceptor. *Cell*. 2000;103:525–35.
- Takayama Y, Shibasaki K, Suzuki Y, Yamanaka A, and Tominaga M. Modulation of water efflux through functional interaction between TRPV4 and TMEM16A/anoctamin 1. *FASEB J*. 2014;28:2238–48.
- Toft-Bertelsen TL, MacAulay N. TRPV4 to the point of clarity: understanding the function of the complex TRPV4 ion channel. *Cells*. 2021;10:165.
- Preston D, Simpson S, Halm D, Hochstetler A, Schwerk C, Schroten H, and Blazer-Yost BL. Activation of TRPV4 stimulates transepithelial ion

- flux in a porcine choroid plexus cell line. *Am J Physiol Cell Physiol*. 2018;315:C357–C366.
27. Simpson S, Preston D, Schwerk C, Schroten H, and Blazer-Yost B. Cytokine and inflammatory mediator effects on TRPV4 function in choroid plexus epithelial cells. *Am J Physiol Cell Physiol*. 2019;317:C881–C893.
 28. Hochstetler AE, Smith HM, Preston DC, Reed MM, Territo PR, Shim JW, Fulkerson D, Blazer-Yost BL. TRPV4 antagonists ameliorate ventriculomegaly in a rat model of hydrocephalus. *JCI Insight*. 2020;5:e137646
 29. Lodhia KR, Shakui P, and Keep RF. Hydrocephalus in a rat model of intraventricular hemorrhage. *Acta Neurochir Suppl*. 2006;96:207–11.
 30. Tanioka H, Shirakawa T, Machida T, and Sasaki Y. Three-dimensional reconstructed MR imaging of the inner ear. *Radiology*. 1991;178:141–4.
 31. Avants BB, Tustison NJ, Stauffer M, Song G, Wu B, and Gee JC. The Insight ToolKit image registration framework. *Front Neuroinform*. 2014;8:44.
 32. Tustison NJ, Avants BB, Cook PA, Zheng Y, Egan A, Yushkevich PA, and Gee JC. N4ITK: improved N3 bias correction. *IEEE Trans Med Imaging*. 2010;29:1310–20.
 33. Yushkevich PA, Piven J, Hazlett HC, Smith RG, Ho S, Gee JC, and Gerig G. User-guided 3D active contour segmentation of anatomical structures: significantly improved efficiency and reliability. *Neuroimage*. 2006;31:1116–28.
 34. Beddek K, Raffin F, Borgel D, Saller F, Riccobono D, Bobe R, and Boittin FX. TRPV4 channel activation induces the transition of venous and arterial endothelial cells toward a pro-inflammatory phenotype. *Physiol Rep*. 2021;9:e14613.
 35. Dobin A, Davis CA, Schlesinger F, Drenkow J, Zaleski C, Jha S, Batut P, Chaisson M, and Gingeras TR. STAR: ultrafast universal RNA-seq aligner. *Bioinformatics*. 2013;29:15–21.
 36. Abrams ZB, Johnson TS, Huang K, Payne PRO, and Coombes K. A protocol to evaluate RNA sequencing normalization methods. *BMC Bioinformatics*. 2019;20:679.
 37. Li B and Dewey CN. RSEM: accurate transcript quantification from RNA-Seq data with or without a reference genome. *BMC Bioinformatics*. 2011;12:323.
 38. Lolanssen SD, Rostgaard N, Andreassen SN, Simonsen AH, Juhler M, Has-selbalch SG, and MacAulay N. Elevated CSF inflammatory markers in patients with idiopathic normal pressure hydrocephalus do not promote NKCC1 hyperactivity in rat choroid plexus. *Fluids Barriers CNS*. 2021;18:54.
 39. Xin J, Mark A, Afrasiabi C, Tsueng G, Juchler M, Gopal N, Stupp GS, Putman TE, Ainscough BJ, Griffith OL, Torkamani A, Whetzel PL, Mungall CJ, Mooney SD, Su AI, and Wu C. High-performance web services for querying gene and variant annotation. *Genome Biol*. 2016;17:91.
 40. Wu C, Macleod I, and Su AI. BioGPS and MyGene.info: organizing online, gene-centric information. *Nucleic Acids Res*. 2013;41:D561–5.
 41. Carbon S, Ireland A, Mungall CJ, Shu S, Marshall B, Lewis S, Ami GOH, and Web Presence Working G. AmiGO: online access to ontology and annotation data. *Bioinformatics*. 2009;25:288–9.
 42. Day-Richter J, Harris MA, Haendel M, Gene Ontology OBOEWF, Lewis S. OBO-edit—an ontology editor for biologists. *Bioinformatics*. 2007;23:2198–200.
 43. Mi H, Muruganujan A, Ebert D, Huang X, and Thomas PD. PANTHER version 14: more genomes, a new PANTHER GO-slim and improvements in enrichment analysis tools. *Nucleic Acids Res*. 2019;47:D419–D426.
 44. Alexander SP, Mathie A, Peters JA, Veale EL, Striessnig J, Kelly E, Armstrong JF, Faccenda E, Harding SD, Pawson AJ, Southan C, Davies JA, Aldrich RW, Attali B, Baggetta AM, Becirovic E, Biel M, Bill RM, Catterall WA, Conner AC, Davies P, Dellling M, Virgilio FD, Falzoni S, Fenske S, George C, Goldstein SAN, Grissmer S, Ha K, Hammelmann V, Hanukoglu I, Jarvis M, Jensen AA, Kaczmarek LK, Kellenberger S, Kennedy C, King B, Kitchen P, Lynch JW, Perez-Reyes E, Plant LD, Rash L, Ren D, Salzman MM, Sivilotti LG, Smart TG, Snutch TP, Tian J, Trimmer JS, Van den Eynde C, Vriens J, Wei AD, Winn BT, Wulff H, Xu H, Yue L, Zhang X, and Zhu M. THE CONCISE GUIDE TO PHARMACOLOGY 2021/22: Ion channels. *Br J Pharmacol*. 2021;178 Suppl 1:S157–S245.
 45. Kanehisa M, Goto S. KEGG: Kyoto encyclopedia of genes and genomes. *Nucleic Acid Res*. 2000;28:27–30.
 46. Szklarczyk D, Gable AL, Lyon D, Junge A, Wyder S, Huerta-Cepas J, Simonovic M, Doncheva NT, Morris JH, Bork P, Jensen LJ, and Mering CV. STRING v11: protein-protein association networks with increased coverage, supporting functional discovery in genome-wide experimental datasets. *Nucleic Acids Res*. 2019;47:D607–D613.
 47. Soderberg O, Gullberg M, Jarvius M, Ridderstrale K, Leuchowius KJ, Jarvius J, Wester K, Hydbring P, Bahram F, Larsson LG, and Landegren U. Direct observation of individual endogenous protein complexes in situ by proximity ligation. *Nat Methods*. 2006;3:995–1000.
 48. Keep RF, Xiang J, and Betz AL. Potassium cotransport at the rat choroid plexus. *Am J Physiol*. 1994;267:C1616–22.
 49. Toft-Bertelsen TL, Krizaj D, and MacAulay N. When size matters: transient receptor potential vanilloid 4 channel as a volume-sensor rather than an osmo-sensor. *J Physiol*. 2017;595:3287–3302.
 50. Beaudet L, Rodriguez-Suarez R, Venne M-H, Caron M, Bédard J, Brechler V, Parent S, and Bielefeld-Sévigny M. AlphaLISA immunoassays: the no-wash alternative to ELISAs for research and drug discovery. *Nature Methods*. 2008;5:an8-an9.
 51. Andreassen SN, Toft-Bertelsen TL, Wardman JH, Villadsen R, MacAulay N. Transcriptional profiling of transport mechanisms and regulatory pathways in rat choroid plexus. *Fluids Barriers CNS*. 2022;19:44.
 52. Vincent F, Acevedo A, Nguyen MT, Dourado M, DeFalco J, Gustafson A, Spiro P, Emerling DE, Kelly MG, and Duncon M. Identification and characterization of novel TRPV4 modulators. *Biochem Biophys Res Commun*. 2009;389:490–4.
 53. Lykke K, Tollner K, Feit PW, Erker T, MacAulay N, and Loscher W. The search for NKCC1-selective drugs for the treatment of epilepsy: Structure-function relationship of bumetanide and various bumetanide derivatives in inhibiting the human cation-chloride cotransporter NKCC1A. *Epilepsy Behav*. 2016;59:42–9.
 54. Park S, Ku SK, Ji HW, Choi JH, and Shin DM. Ca(2+) is a regulator of the WNK/OSR1/NKCC pathway in a human salivary gland cell line. *Korean J Physiol Pharmacol*. 2015;19:249–55.
 55. Zhang J, Deng X, and Kahle KT. Leveraging unique structural characteristics of WNK kinases to achieve therapeutic inhibition. *Sci Signal*. 2016;9:e3.
 56. Cinalli G, Spennato P, Nastro A, Aliberti F, Trischitta V, Ruggiero C, Mirone G, and Cianciulli E. Hydrocephalus in aqueductal stenosis. *Childs Nerv Syst*. 2011;27:1621–42.
 57. Beni-Adani L, Biani N, Ben-Sirah L, and Constantini S. The occurrence of obstructive vs absorptive hydrocephalus in newborns and infants: relevance to treatment choices. *Childs Nerv Syst*. 2006;22:1543–63.
 58. Oi S and Di Rocco C. Proposal of “evolution theory in cerebrospinal fluid dynamics” and minor pathway hydrocephalus in developing immature brain. *Childs Nerv Syst*. 2006;22:662–9.
 59. Rekatte HL. The definition and classification of hydrocephalus: a personal recommendation to stimulate debate. *Cerebrospinal Fluid Res*. 2008;5:2.
 60. Karimiy JK, Reeves BC, Damisah E, Duy PQ, Antwi P, David W, Wang K, Schiff SJ, Limbrick DD, Jr., Alper SL, Warf BC, Nedergaard M, Simard JM, and Kahle KT. Inflammation in acquired hydrocephalus: pathogenic mechanisms and therapeutic targets. *Nat Rev Neurol*. 2020;16:285–296.
 61. Relkin N, Marmarou A, Klinge P, Bergsneider M, and Black PM. Diagnosing idiopathic normal-pressure hydrocephalus. *Neurosurgery*. 2005;57:54–16; discussion ii-v.
 62. Williams MA, Malm J. Diagnosis and treatment of idiopathic normal pressure hydrocephalus. *Continuum*. 2016;22:579–99.
 63. Lolanssen SD, Rostgaard N, Barbuskaite D, Capion T, Olsen MH, Norager NH, Vilhardt F, Andreassen SN, Toft-Bertelsen TL, Ye F, Juhler M, Keep RF, MacAulay N. Posthemorrhagic hydrocephalus associate with elevated inflammation and CSF hypersecretion via activation of choroidal transporters. *Fluids Barriers CNS*. 2022; in press.
 64. Atlas AB. <http://www.brain-map.org>.
 65. Bothwell SW, Omileke D, Patabendige A, Spratt NJ. CSF secretion is not altered by NKCC1 nor TRPV4 antagonism in healthy rats. *Brain Sci*. 2021;11:1117.
 66. Kahle KT, Rinehart J, and Lifton RP. Phosphoregulation of the Na-K-2Cl and K-Cl cotransporters by the WNK kinases. *Biochim Biophys Acta*. 2010;1802:1150–8.
 67. Piechotta K, Lu J, and Delpire E. Cation chloride cotransporters interact with the stress-related kinases Ste20-related proline-alanine-rich kinase (SPAK) and oxidative stress response 1 (OSR1). *J Biol Chem*. 2002;277:50812–9.
 68. Ohuchi H, Hamada A, Matsuda H, Takagi A, Tanaka M, Aoki J, Arai H, and Noji S. Expression patterns of the lysophospholipid receptor genes during mouse early development. *Dev Dyn*. 2008;237:3280–94.
 69. Zhang J, Bhuiyan MIH, Zhang T, Karimiy JK, Wu Z, Fiesler VM, Zhang J, Huang H, Hasan MN, Skrzypiec AE, Mucha M, Duran D, Huang W, Pawlak R, Foley LM, Hitchens TK, Minnigh MB, Poloyac SM, Alper SL, Molyneux BJ, Trevelyan AJ, Kahle KT, Sun D, and Deng X. Modulation of brain cation-Cl(-) cotransport via the SPAK kinase inhibitor ZT-1a. *Nat Commun*. 2020;11:78.

70. Huang H, Song S, Banerjee S, Jiang T, Zhang J, Kahle KT, Sun D, Zhang Z. The WNK-SPAK/OSR1 kinases and the cation-chloride cotransporters as therapeutic targets for neurological diseases. *Aging Dis.* 2019;10:626–36.
71. Uggeri J, Gatti R, Silvana B, Scandroglio R, Corradini R, Rotoli BM, and Orlandini G. Calcein-AM is a detector of intracellular oxidative activity. *Histochem. Cell Biol.* 2004;122:499–505.

Publisher's Note

Springer Nature remains neutral with regard to jurisdictional claims in published maps and institutional affiliations.

Ready to submit your research? Choose BMC and benefit from:

- fast, convenient online submission
- thorough peer review by experienced researchers in your field
- rapid publication on acceptance
- support for research data, including large and complex data types
- gold Open Access which fosters wider collaboration and increased citations
- maximum visibility for your research: over 100M website views per year

At BMC, research is always in progress.

Learn more biomedcentral.com/submissions

